Physics and Chemistry of the Earth 123 (2021) 103002

Contents lists available at ScienceDirect

Physics and Chemistry of the Earth

journal homepage: http://www.elsevier.com/locate/pce

Joint inversion of ground gravity data and satellite gravity gradients between Nepal and Bhutan: New insights on structural and seismic segmentation of the Himalayan arc

Rodolphe Cattin [a,*], Théo Berthet [b], György Hetényi [c], Anita Saraswati [a,d], Isabelle Panet [e,f], Stéphane Mazzotti [a], Cécilia Cadio [a], Matthieu Ferry [a]

[a] Géosciences Montpellier, Université de Montpellier, CNRS, Montpellier, France
[b] Department of Earth Sciences, Uppsala University, Villavägen 16, 75236, Uppsala, Sweden
[c] Institute of Earth Sciences, University of Lausanne, Géopolis, Quartier UNIL-Mouline, 1015, Lausanne, Switzerland
[d] Faculty of Sciences, Technology and Medicine, Université du Luxembourg, L-4364, Esch-sur-Alzette, Luxembourg
[e] Université de Paris, Institut de physique du globe de Paris, CNRS, IGN, F-75005, Paris, France
[f] ENSG-Géomatique, IGN, F-77455, Marne-la-Vallée, France

ARTICLE INFO

Keywords:
Himalaya
Segmentation
Bouguer anomaly
GOCE gradients

ABSTRACT

Along-strike variation in the geometry of lithospheric structures is a key control parameter for the occurrence and propagation of major interplate earthquakes in subduction and collision zones. The lateral segmentation of the Himalayan arc is now well-established from various observations, including topography, gravity anomalies, exhumation rates, and present-day seismic activity. Good knowledge of the main geometric features of these segments and their boundaries is thus the next step to improve seismic hazard assessment in this area. Following recent studies, we focus our approach on the transition zone between Nepal and Bhutan where both M > 8 earthquakes and changes in the geometry of the Indian plate have been documented. Ground gravity data sets are combined with satellite gravity gradients provided by the GOCE mission (Gravity Field and Steady-State Ocean Circulation Explorer) in a joint inversion to assess the location and the geometry of this transition. We obtain a ca. 10 km wide transition zone located at the western border of Bhutan that is aligned with the Madhupur fault in the foreland and coincides with the Dhubri–Chungthang fault zone and the Yadong-Gulu rift in Himalaya and southern Tibet, respectively. This sharp segment boundary at depth can act as a barrier to earthquake rupture propagation. It can possibly restrict the size of large earthquakes and thus reduce the occurrence probability of M > 9 earthquakes along the Main Himalayan Thrust.

1. Introduction

It is well-established that along-strike variations of megathrusts in both subduction and collision zones are key parameters which control the location and size of major earthquakes.

Over the last two decades, several great earthquakes (M > 8) have been documented in Himalayas along the Main Frontal Thrust (MFT) from paleoseismic studies (e.g. Nakata et al., 1998; Lavé et al., 2005; Kumar et al., 2010; Mugnier et al., 2013; Sapkota et al., 2013; Bollinger et al., 2014; Rajendran et al., 2015; Le Roux–Mallouf et al., 2016, 2020; Wesnousky et al., 2017a, b, 2018, 2019). Lavé et al. (2005) suggested that at least one great earthquake with an estimated vertical slip component of 7–7.5 m (and an inferred total coseismic displacement on the order of 17 m) ruptured a large segment of the Himalayan arc around 1100 in central Nepal. Further east, Sapkota et al. (2013) documented at least one great earthquake before 1300 with an estimated vertical slip component between 3 m and 8 m (and an inferred total coseismic displacement between 5 m and 17 m). Additionally, Kumar et al. (2010) described co-seismic displacements larger than 12 m both East and West of Bhutan, with possibly contemporaneous age constraints. Le Roux-Mallouf et al. (2016) documented also a great earthquake in Bhutan which occurred between 1140 and 1520 with ~8 m of vertical offset. More recently, Wesnousky et al. (2017b, 2018, 2019) completed this catalog by studying three sites in central eastern Nepal showing vertical coseismic slip of about 7 m compatible with an earthquake in ca. 1100 (Fig. 1).

* Corresponding author.
E-mail address: rodolphe.cattin@umontpellier.fr (R. Cattin).

https://doi.org/10.1016/j.pce.2021.103002
Received 16 September 2020; Received in revised form 11 December 2020; Accepted 11 February 2021
Available online 16 March 2021

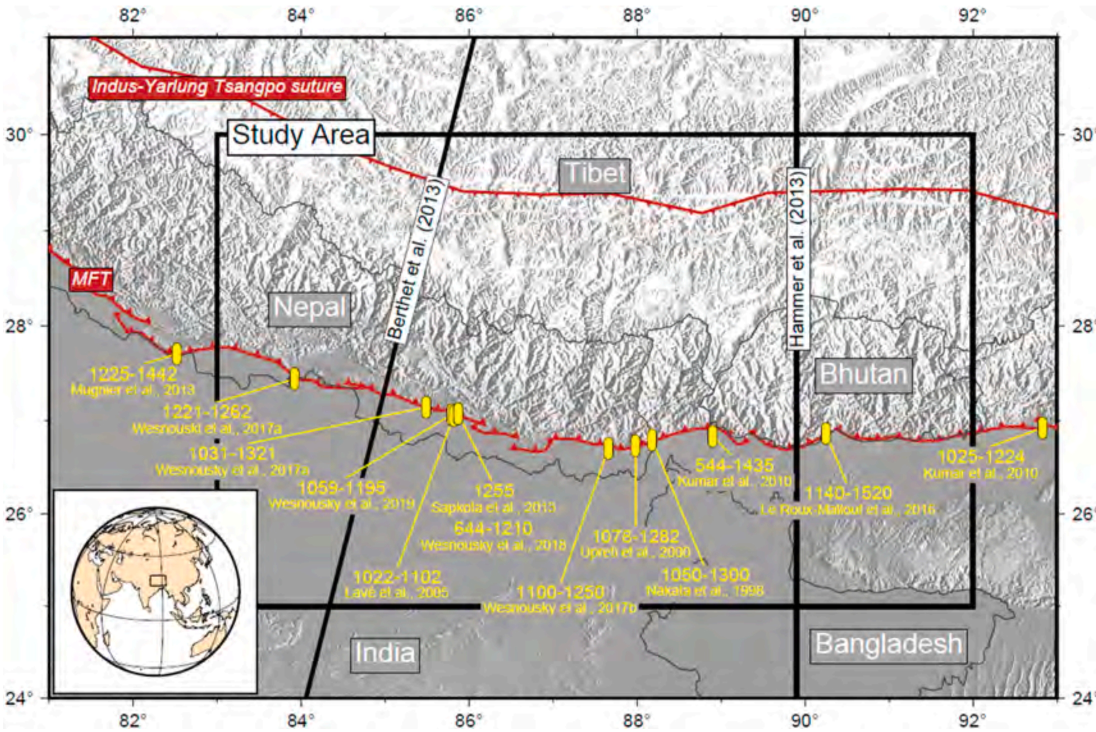

Fig. 1. Elevation map of the Himalayas and surrounding regions. Yellow rectangles give the location of medieval earthquake study sites along the Main Frontal Thrust (MFT) modified from Wesnousky et al. (2019). Sites are labeled to show the age of paleoearthquakes and authors reporting results. Black contour is the limit of our study area. Boundaries of India, Bangladesh, Nepal, Bhutan, and Tibet as well as major tectonic structures (MFT and Indus-Yarlung Tsangpo suture) are shown as reference. Black lines show the locations of profiles studied by Berthet et al. (2013) and Hammer et al. (2013).

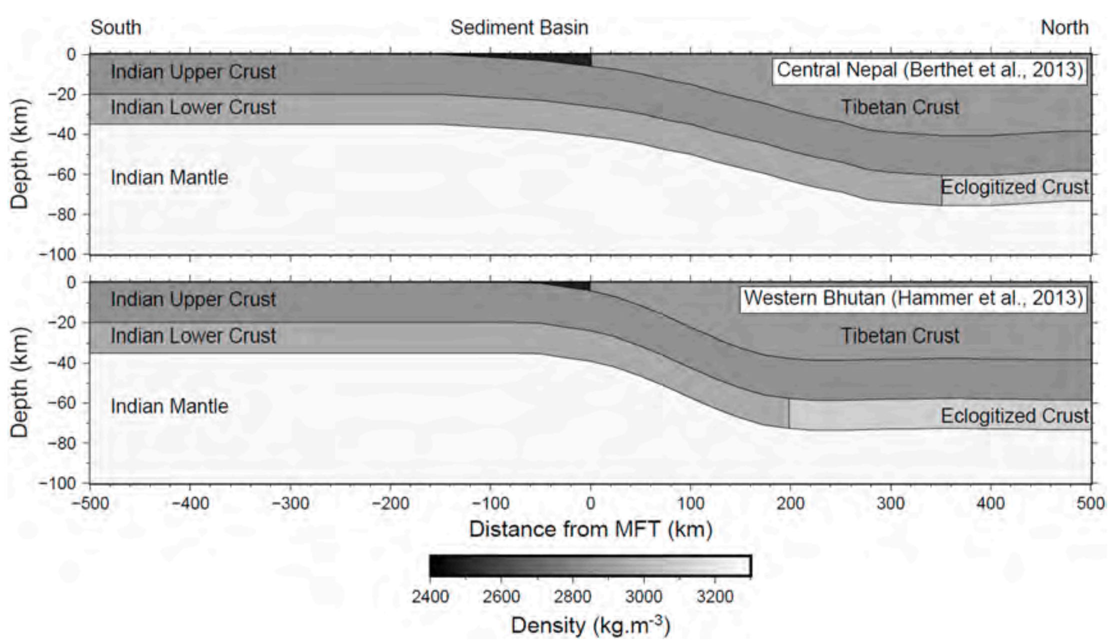

Fig. 2. Geometry and density structure of the lithosphere in central Nepal and western Bhutan (see location Fig. 1). These two profiles are inferred from Bouguer anomalies, receiver functions, and boreholes data acquired across the Himalaya from India to Tibet (Berthet et al., 2013; Hammer et al., 2013). They include sediment basin, Tibetan crust, and Indian plate, which is composed of three layers: upper crust, lower crust (eclogitized beneath Tibet), and lithospheric mantle.

During the same period, many studies in thermochronology, geomorphology and geophysics have revealed the segmented nature of the Himalayan arc in terms of along-strike variations of tectonic structures (e.g. Duncan et al., 2003; Robert et al., 2011; Hetényi et al., 2016; Dal Zilio et al., 2020). However, the main geometric features of the boundaries of these segments remain poorly constrained. For instance, Duncan et al. (2003) showed a clear difference in the topographic profiles across central Nepal and Bhutan. Based on low temperature thermochronology data and associated exhumation rates, Robert et al. (2011) suggested also along-strike variations in the geometry of crustal-scale faults between central Nepal and Bhutan. These two studies are focused on individual sections across the belt and do not provide

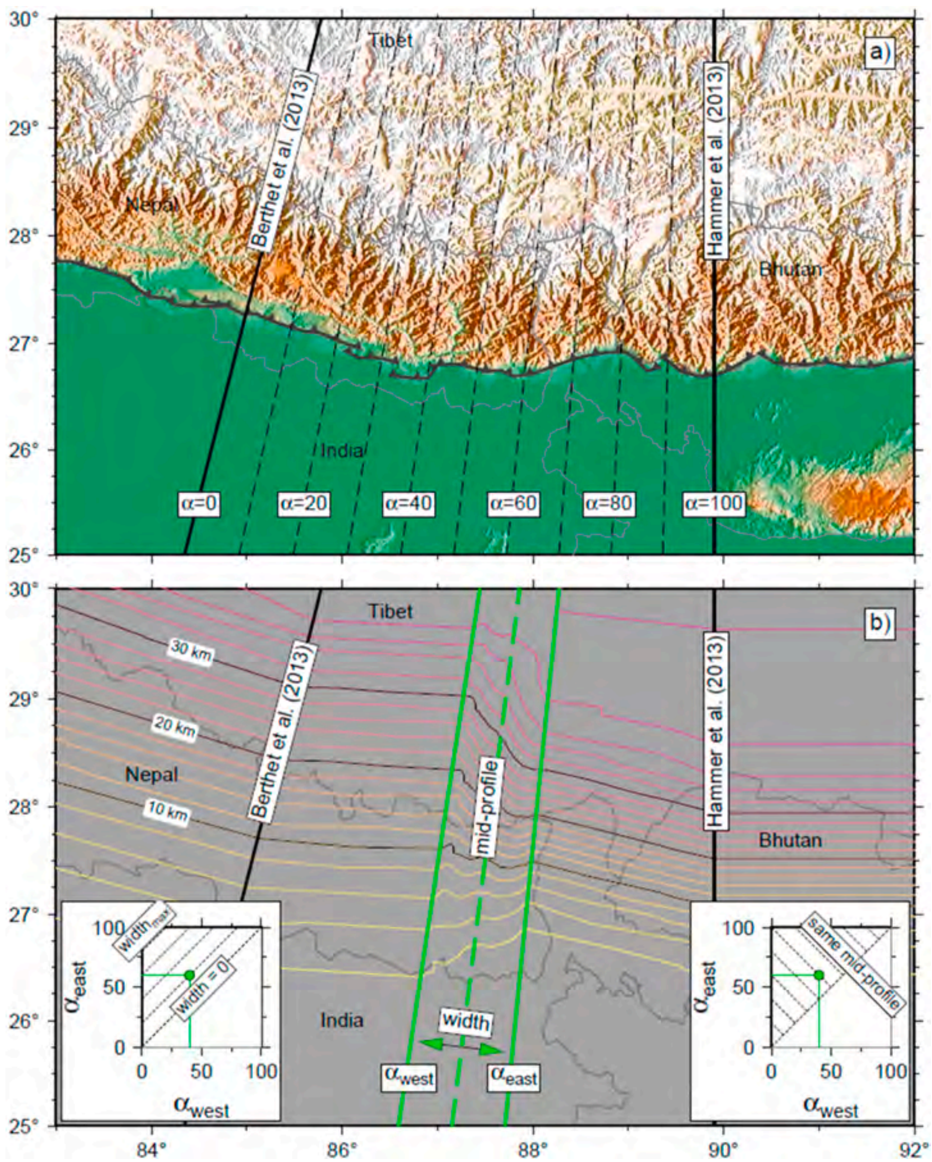

Fig. 3. Method adopted to investigate the lateral variation of lithospheric structures between central Nepal and western Bhutan. (a) Topographic map showing the location of considered profiles. α is a weighting coefficient between the two previously studied profiles of central Nepal and western Bhutan. $\alpha = 0$ and $\alpha = 100$ are associated with the profile of Berthet et al. (2013) and Hammer et al. (2013), respectively. (b) Color contours show the modelled depth of the top of the downgoing Indian upper crust, which is defined from the two profiles depicted in Fig. 2 and from the transition zone bound by $\alpha_{west} = 40$ and $\alpha_{east} = 60$ (green lines). Left inset: Dashed lines parallel to the first bisector ($\alpha_{east} - \alpha_{west} = constant$) are associated with transition zones of similar width. Right inset: Dashed lines perpendicular to the first bisector represent transition zones with a similar mid-profile location ($[\alpha_{east} + \alpha_{west}]/2 = constant$).

information about the transition itself, neither on its location nor on its width.

This lack of information represents a major limitation for seismic hazard assessment along the Himalayan arc and prevents any interpretation of past major earthquake sequences in terms of geometric segmentation. In this study, we focus on the area between central Nepal and Bhutan, where major lateral variations as well as seismic segmentation have been already documented. First, we fix the lithospheric structure's geometry of each segment from available 2D images of the underthrusting Indian plate across central Nepal and western Bhutan. Next, after synthetic tests, we assess the main geometric features of this boundary from a joint approach using both ground and satellite gravity data sets. Finally, we discuss the structural control of this segment boundary on present-day deformation and its relationship with the propagation of major historical earthquakes between Nepal and Bhutan.

2. Method and data

2.1. Evidences of along-strike discontinuity

Although the tectonic units are remarkably continuous along the 2400 km long shape of the Himalayas, a growing number of studies suggest the existence of lateral variations, especially between central Nepal and Bhutan. Duncan et al. (2003) were the first to highlight along-strike variations by showing differences in the patterns of topographic profiles between Nepal and Bhutan. Since this pioneering study, detailed geologic mapping and thermochronological data have underlined along-strike changes in the stratigraphy and structure between these two regions (e.g. McQuarrie et al., 2008; Robert et al., 2011). Based on geophysical information, Gahalaut and Arora (2012) propose a control of these inherited structures on seismic segmentation marked by a low present-day seismicity rate in Bhutan compared to the Nepal segment. The analysis of arc-parallel gravity anomalies highlights also lateral variations in the geometry of the foreland basin as well as in the deep structure of the orogen between Nepal and Bhutan (Hetényi et al., 2016). More recently, Dal Zilio et al. (2020) show a clear zonation of interseismic coupling inferred from geodetic data, with a high coupling of ca. 0.8 in Nepal compared to ca. 0.5 in western and central Bhutan.

2.2. Approach strategy

No studies to date, however, have focused on the main geometric features of this transition zone between central and eastern Himalaya. First, to better assess its precise location as well as its lateral extension,

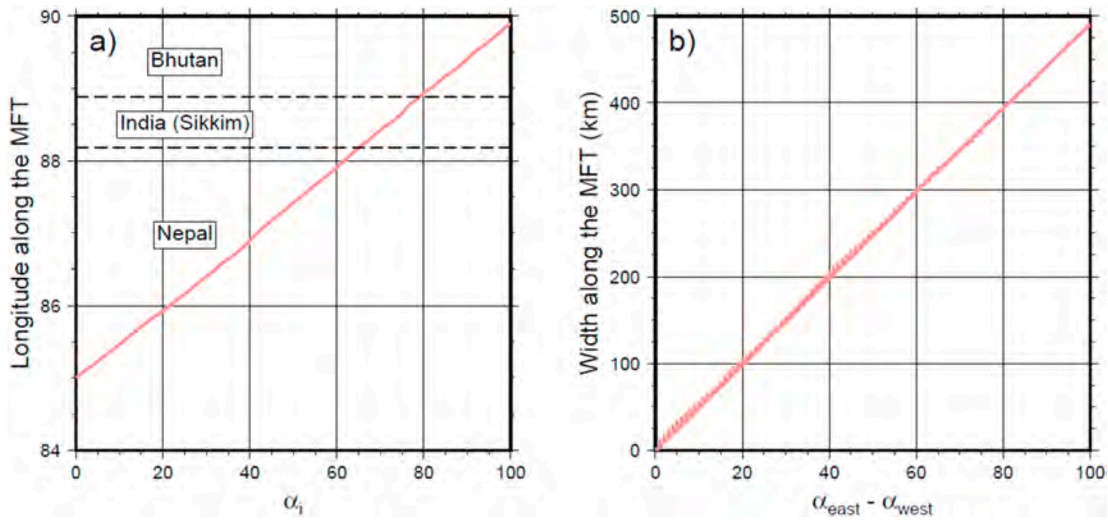

Fig. 4. Relationship between the assumed coefficient α and the main features of the tested transition zone. (a) Geographic location of the study profiles given by their longitude along the Main Frontal Thrust (MFT). α_i refers either to α_{east}, α_{west} or $\alpha_{mid-profile} = [\alpha_{west} + \alpha_{east}]/2$. (b) Width of the transition zone along the MFT. Distances are obtained assuming that the points lie on the WGS84 reference ellipsoid.

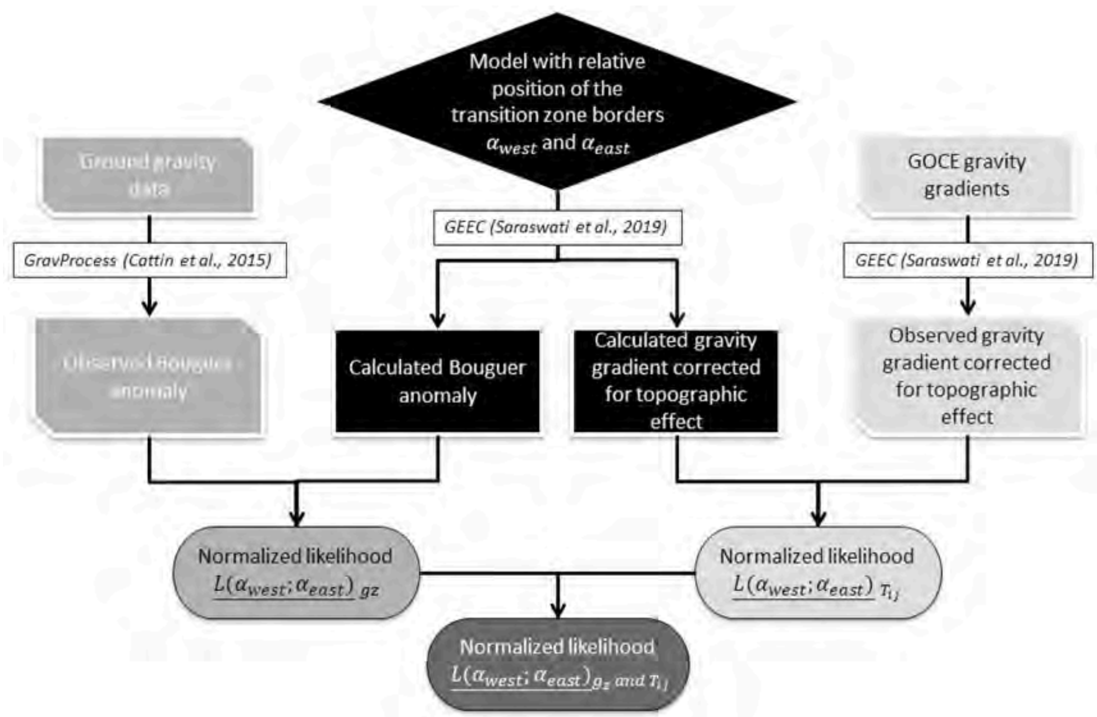

Fig. 5. Flow chart for both data processing and models likelihood calculation. Ground gravity data are fully processed using the GravProcess software (Cattin et al., 2015) to obtain Bouguer anomaly. GOCE data reduction (topographic effect) is performed using the GEEC software with WGS84 as the reference ellipsoid (Saraswati et al., 2019). We define a model geometry for the study transition zone using coefficients α_{west} and α_{east} for the relative position of its western and eastern boundaries (see Fig. 3). The associated likelihood is obtained from the comparison between the calculated and the observed Bouguer anomaly or gravity gradients and ultimately both. The inversion is then performed with a systematic exploration of the coefficients α_{west} and α_{east} in a range between 0 and 100 with a step of 1.

we consider two master profiles across the range:

- For the Nepal segment, many structural geology field campaigns as well as seismological experiments were performed to image the main structures (e.g. Le Fort, 1975; Schulte-Pelkum et al., 2005; Nábělek et al., 2009). The geometry of major faults, the depth of both the Moho and the foreland sedimentary basin as well as the physical properties of crust and mantle are now relatively well-known. In the following, we use the results obtained by Berthet et al. (2013) from ground gravity measurements in Nepal between longitude 83° and 86.5°. This profile (BP hereinafter) is a cross-section through the range at the longitude of Kathmandu (see location Fig. 1). This profile is consistent with previous geological and seismological results and provides information about density layering (Fig. 2).
- For the Bhutan segment, fewer studies have been conducted. Nevertheless, recent thermochronological data (e.g. McQuarrie et al., 2008, 2015; Coutand et al., 2014), geomorphological observations (Le Roux-Mallouf et al., 2015) and geophysical works

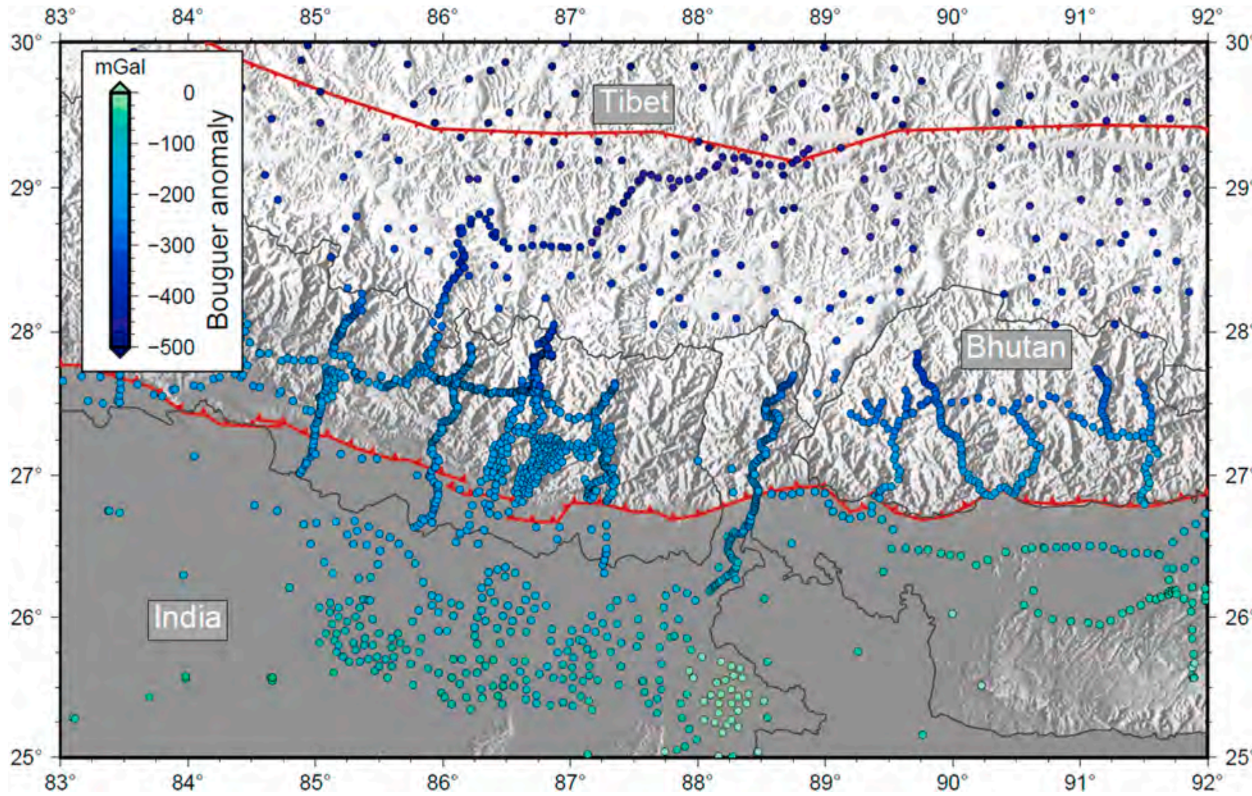

Fig. 6. Bouguer anomaly map of the Himalayas and surrounding regions. Color circles are associated with the gravity dataset compiled by Hetényi et al. (2016) from the International Gravimetric Bureau database (BGI, http://bgi.omp.obs-mip.fr/) and previous studies (Das et al., 1979; Sun, 1989; Banerjee, 1998; Cattin et al., 2001; Tiwari et al., 2006; Hammer et al., 2013; Berthet et al., 2013). Boundaries of countries, geographic regions and the main tectonic structures are shown as reference.

(Hammer et al., 2013; Singer et al., 2017; Diehl et al., 2017) allow constraining the geometry of deep structures in west-central Bhutan. In the following, we use the profile obtained by Hammer et al. (2013) from ground gravity measurements (Fig. 2). This profile (HP hereinafter) is a cross-section through the range at the longitude of the city of Wangdue Phodrang (see location Fig. 1).

These two model profiles (HP and BP) have many similarities: a comparable north-south extension, the bending of the Indian plate under Tibet associated with an eclogitization of the Indian lower crust, and an identical Moho depth under central Tibet. They also have their own characteristics with a smaller and shallower foreland basin, a shorter flexural wavelength, and a eclogitized zone reaching further south in Bhutan compared to Nepal (Fig. 2), although this feature is included in a simplified way in both models compared to a petrologically constrained model presented in Hetényi et al. (2007).

Second, to extend laterally these two profiles, we use additional cross-sections defined with a weighting coefficient α between Berthet's and Hammer's profiles:

$$(long, lat)_{profile} = \frac{1}{100}\left[(100-\alpha)\times(long, lat)_{BP} + \alpha\times(long, lat)_{HP}\right] \quad (1)$$

where *long* is the longitude and *lat* the latitude of points of profiles. $\alpha = 0$ and $\alpha = 100$ are associated with BP and HP, respectively (Fig. 3a). Next, we define α_{west} and α_{east} for the relative position of the eastern and the western boundaries of the transition zone. Assuming that the transition zone is located between BP and HP, these two coefficients range between 0 and 100 and by definition $\alpha_{west} < \alpha_{east}$. In a $(\alpha_{west}, \alpha_{east})$ diagram, the lines parallel to the first bisector ($\alpha_{east} - \alpha_{west} = constant$) are associated with transition zones with the same width, whereas the lines perpendicular to the first bisector are related to transition zones with the same mid-profile ($[\alpha_{east} + \alpha_{west}]/2 = constant$). Although a linear relationship exists between the α coefficients and the geometry properties of the transition zone (Fig. 4), in the following we will use these coefficients because they are more suitable for defining a 3D geometry. We create a mesh model assuming a lateral uniformity between $\alpha = 0$ and α_{west} as well as between α_{east} and $\alpha = 100$. We consider a linear interpolation between α_{west} and α_{east} using 10 profiles to create a locally refined mesh for the transition zone (Fig. 3b). Two additional far-field profiles are used to reduce boundary effects.

Finally, the gravity effect due to the meshed lithospheric bodies is calculated using the GEEC software, which enables to compute both the gravity field and the full-tensor gravity gradient due to irregularly shaped body mass (Saraswati et al., 2019). The results obtained by varying α_{west} and α_{east} are then compared with gravity data sets, which include ground Bouguer anomaly measurements and satellite gravity gradients (see flow chart on Fig. 5).

2.3. Ground gravity data set

The terrestrial gravity data set used in this study comes from the compilation published by Hetényi et al. (2016). It was based on already available data from the International Gravimetric Bureau (BGI, http://bgi.omp.obs-mip.fr/) and published studies (Das et al., 1979, Sun, 1989; Banerjee, 1998, Martelet et al., 2001, Tiwari et al., 2006). This data set has been completed with field measurements performed in Nepal (Berthet et al., 2013) and Bhutan (Hammer et al., 2013) for obtaining a better coverage on either side of the Himalayas as well as more than 10 profiles across the mountain belt (Fig. 1). All the data sets have been fully reprocessed in the same manner using the GravProcess software (Cattin et al., 2015), resulting in a coherent data set of 2749 Bouguer anomalies g_Z (Fig. 6). Together with the errors in the vertical position and the low resolution of the SRTM digital elevation model in high relief

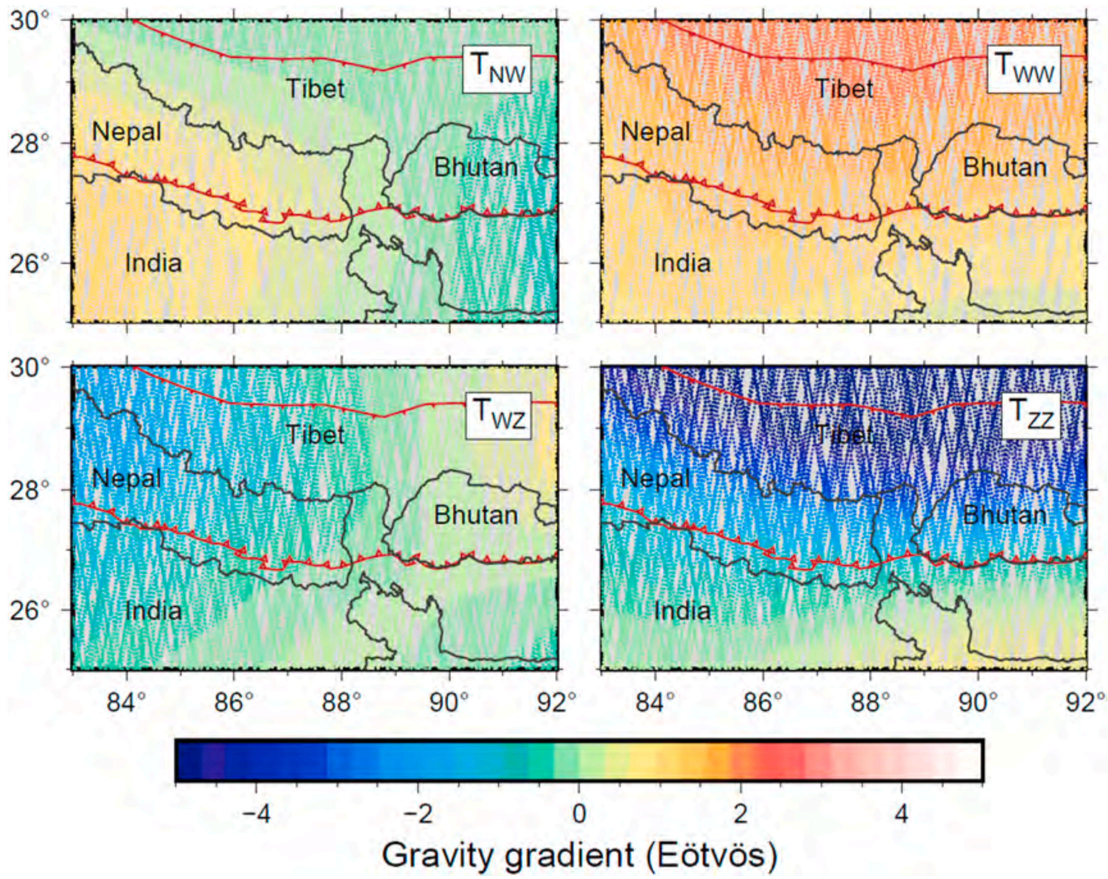

Fig. 7. Map of gravity gradients including topographic corrections from the spatial gravity mission GOCE (Gravity Field and Steady-State Ocean Circulation Explorer). Color dots represent data along the satellite orbits at an altitude between 225 km and 265 km. T_{ij} is the ij component of gravity gradient tensor. T_{NW}, T_{WW}, and T_{WZ} are associated with the partial derivative of the three gravity components in the west direction. T_{ZZ} is the partial derivative of g_Z in the vertical direction. Borders of countries and the main tectonic structures are shown as reference.

areas, the discrepancy between existing data sets lead to an average accuracy of a few mGal (<10 mGal) for this compilation of ground gravity data.

2.4. GOCE gravity gradients

The satellite data used in this study are the GOCE (Gravity Field and Steady-State Ocean Circulation Explorer) gravity gradients of level-2 product EGG_TRF_2 (https://goce-ds.eo.esa.int/oads/access/). This type of data sets has been externally calibrated and corrected to temporal gravity variations by the GOCE High Processing Facility (HPF) (Gruber et al., 2011). The gravity gradients are provided in the Local North Oriented Frame (LNOF, see Fuchs and Bouman, 2011). To maximize the signal-to-noise ratio, we consider the period between August 2012 and September 2013, for which the satellite operated in low orbit at an altitude as low as 224 km.

To assess the signal due to variations of structures at depth, we perform data reductions (topographic effect) using the GEEC software with WGS84 as the reference ellipsoid (Saraswati et al., 2019). Following this previous study, we consider a digital elevation for the entire Earth with a resolution of 15 km, which we found as a good compromise between the computation time and the result accuracy. These reductions are performed on data along the GOCE orbit to avoid noise amplification due to the downward continuation to the Earth's surface.

The final satellite data set consists of 17,533 measurements of the nine components of gravity gradient tensor $T_{ij} = \partial g_i / \partial x_j$. This tensor is symmetric, its trace is zero and we will focus on the longitudinal variations along the Himalayan arc. Hence, in the following, we will only consider four components that are T_{NW}, T_{WW}, T_{WZ}, and T_{ZZ} (Fig. 7), where *N*, *W* and *Z* are associated with the North-West-Up local frame. Taking into account the uncertainties in the measurements and the errors associated with both the ellipsoid model and the digital elevation model, an average accuracy of 0.1 E is assumed hereinafter for the derived gravity gradient anomalies (which are Bouguer anomalies).

3. Synthetic tests

In this section, we perform tests on synthetic models to assess how our approach allows finding the geometry of a lateral crustal ramp located between the profiles of Berthet et al. (2013) and Hammer et al. (2013). Using the gravity data sets described above, a systematic exploration of the coefficients α_{west} and α_{east} are carried out to test the sensitivity of our inversion results to the transition zone geometry parameters (location and width) as well as to the data uncertainties.

3.1. Synthetic inversion reference test

First, we consider a lateral ramp located halfway between Berthet's and Hammer's profiles with a width of ca. 250 km. This model corresponds to assuming $\alpha_{west} = 25$ and $\alpha_{east} = 75$ as initial coefficients. Using the density distribution at depth of BP and HP, the gravity anomalies and the gravity gradients are computed at the location of gravity measurements. A normal distributed random noise is added to these synthetic data sets with a mean of zero and a standard deviation of 10 mGal and 0.1 E for the Bouguer anomaly and gravity gradients, respectively.

The inversion is performed with a systematic exploration of the coefficients α_{west} and α_{east} in a range between 0 and 100 with a step of 1.

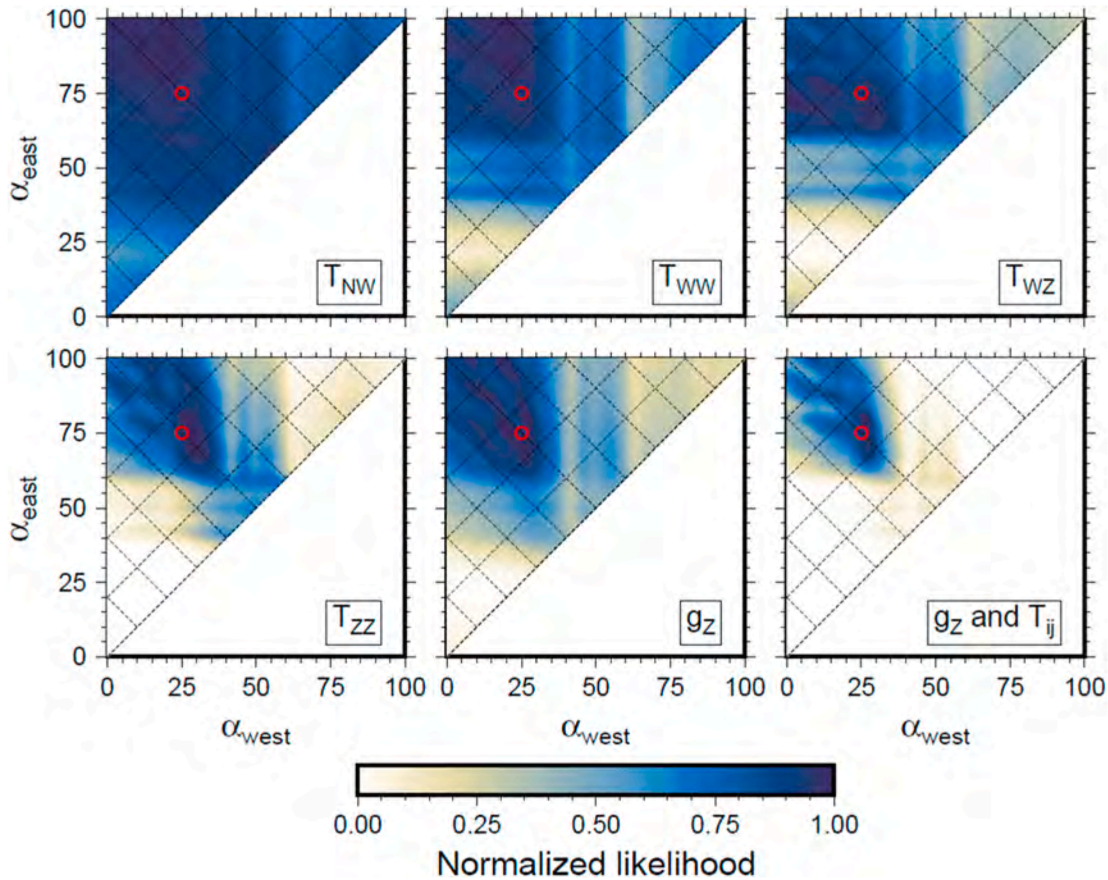

Fig. 8. Synthetic test on gravity and gravity gradients assuming $\alpha_{west} = 25$ and $\alpha_{east} = 75$ as initial coefficients (red circle). The color scale shows for all tested α_{west} and α_{east} values the calculated likelihood obtained either from gravity gradient (T_{NW}, T_{WW}, T_{WZ} and T_{ZZ}), from Bouguer anomaly (g_Z) or from all (g_Z and T_{ij}). This likelihood distribution is normalized with respect to the best-fitting model obtained for each considered dataset. $\sigma_g = 10\ mGal$ and $\sigma_T = 0.1\ E$ are assumed for the standard deviations of gravity and gravity gradient data, respectively.

Knowing that $\alpha_{west} < \alpha_{east}$, for $\alpha_{west} = 0$ we test 100 different $\alpha_{east} \in [1;100]$ values, for $\alpha_{west} = 1$ only 99 values, and so on up to $\alpha_{west} = 99$ for which $\alpha_{east} = 100$. Hence we generate a collection of 5050 models ($\sum_{k=1}^{100} k = \frac{100\times101}{2}$ models) and calculate for each of them their likelihood, which is defined as

$$L(m) = exp\left(-\frac{1}{n}\sum_{i=1}^{n}\left[\frac{calc_i - obs_i}{\sigma_i}\right]^2\right), \tag{2}$$

where n is the number of data, $calc_i$ is the calculated gravity field (either Bouguer anomaly or gravity gradient component), obs_i is the observed gravity field (either Bouguer anomaly or gravity gradient component) and σ_i is the uncertainty, which is fixed to 10 mGal and 0.1 E for the Bouguer anomaly and gravity gradients, respectively.

As shown in Fig. 8, the obtained likelihood distribution is consistent with the initial coefficients $\alpha_{west} = 25$ and $\alpha_{east} = 75$. Our result underlines however the specific nature of each type of data, each providing different constraints on these two coefficients. Not surprisingly, the inversion of T_{NW} measurements gives a mostly constant likelihood because (1) g_N and g_W are low compared to g_Z and (2) the longitudinal variation in g_N or the latitudinal variation in g_W are not significantly affected by a lateral crustal ramp. Although the inversion of either T_{WW} or g_Z underestimates α_{west} and overestimates α_{east}, they provide good information on the location of the mid-profile of the transition zone. In contrast, T_{WZ} and T_{ZZ} are more suitable for finding α_{east} and α_{west}, respectively. Irrespective of which data is used, the width of the transition zone remains poorly constrained.

These results underline the strong nonuniqueness of the gravity inversion. This major limitation can be reduced by a joint inversion, for which the best combinations of α_{west} and α_{east} are obtained using simultaneously all the components of the gravity gradient tensor T_{ij} and the Bouguer anomaly. To give the same weight for all data sets, the likelihood distribution is normalized with the likelihood of the best-fitting model obtained for each data set. So the normalized likelihood $\underline{L}$ ranges between 0 and 1 and the likelihood associated with combined data sets is simply the product of the likelihood obtained from each data set:

$$\underline{L(m)}_{T_{ij}} = \underline{L(m)}_{T_{NW}} \times \underline{L(m)}_{T_{WW}} \times \underline{L(m)}_{T_{Wz}} \times \underline{L(m)}_{T_{ZZ}}\ and\ \underline{L(m)}_{g_z\ and\ T_{ij}} = \underline{L(m)}_{g_z} \times \underline{L(m)}_{T_{ij}} \tag{3}$$

In Fig. 8, the maximum of normalized likelihood ($\underline{L} > 0.9$) is found for $\alpha_{west} = 27 \pm 2$and $\alpha_{east} = 75 \pm 7$. These values are in good agreement with the initial coefficients. This first test demonstrates the consistency of ground gravity data and satellite gravity gradients and the need to invert them together. Furthermore, due to data distribution, this reference test suggests that the western boundary is better constrained than the eastern one (Fig. 8).

3.2. Effect of the lateral extension of the transition zone

In the reference synthetic test we considered a ca. 250 km wide transition zone. Here, we test the influence of this zone's lateral extent in a range between ca. 2.5 km and ca. 490 km, all other parameters

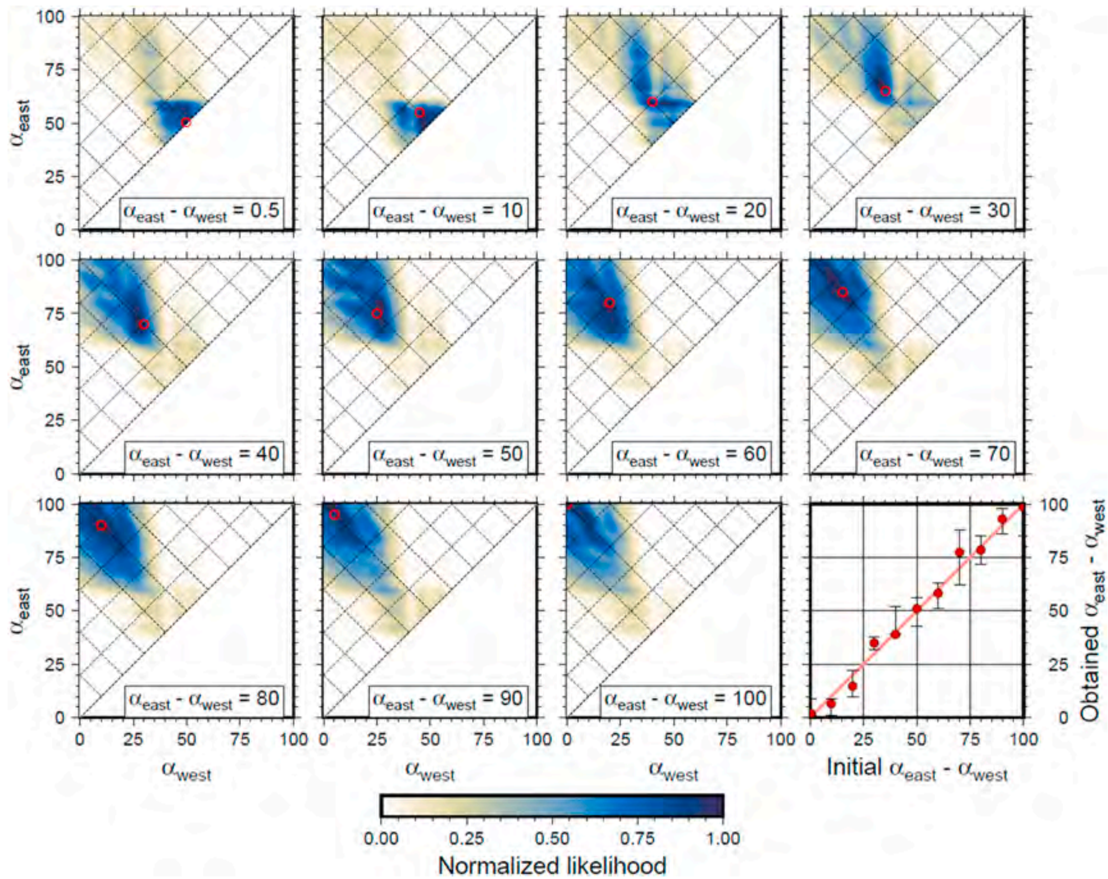

Fig. 9. Synthetic tests assuming for the transition zone a constant mid-profile location ($[\alpha_{east} + \alpha_{west}]/2 = 50$) and widths ranging between ca. 2.5 km ($\alpha_{east} - \alpha_{west} = 0.5$) and ca. 490 km ($\alpha_{east} - \alpha_{west} = 100$). The color scale shows the calculated likelihood distribution obtained from both gravity gradients and Bouguer anomaly (g_Z and T_{ij}) assuming standard deviations of 0.1 *E* and 10 *mGal*, respectively. The red circle shows the assumed initial coefficients α_{west} and α_{east} of synthetic models. The bottom right figure gives a comparison between the initial and the predicted $\alpha_{east} - \alpha_{west}$ values. The pink line corresponds to the first bisector ($y = x$).

remaining unchanged. Following the approach described in the previous section, we generate synthetic data sets with a constant $\alpha_{mid-profile} = [\alpha_{west} + \alpha_{easst}]/2 = 50$ and $\alpha_{east} - \alpha_{west} \in [0.5; 100]$. We then perform a similar inversion of both gravity and gravity gradient data sets as above with a systematic exploration of the coefficients α_{west} and α_{east}.

Whichever the width considered, the maximum likelihood is obtained for α_{west} and α_{east} close to the initial coefficients (Fig. 9). The average standard deviation of the obtained $\alpha_{east} - \alpha_{west}$ is 6 (ca. 30 km). Our results suggest no obvious relationship between this standard deviation and the lateral extent of the transition zone. Both for a very narrow (<5 km) and a very wide (>450 km) zone a low uncertainty (<10 km) is obtained, while for an average width (ca. 200 km) the standard deviation of this parameter can be significant and reach values up to ca. 75 km (Fig. 9). This uncertainty is probably rather related to the heterogeneous distribution of ground gravity data, which shows a gap in far east Nepal (Fig. 6).

3.3. Influence of the transition zone location

We also study the influence of the location of the transition zone. As for the reference model, we assume a ca. 250 km wide transition zone by testing models with mid-profiles located at different positions between central-eastern Nepal and westernmost Bhutan ($[\alpha_{east} + \alpha_{west}]/2 \in [25; 75]$).

The maximum likelihood for α_{west} and α_{east} coincides well with the initial coefficients (Fig. 10). The standard deviation of the obtained location $[\alpha_{east} + \alpha_{west}]/2$ is 2 on average (ca. 10 km distance along the MFT) and can reach up to 4 (ca. 20 km distance along the MFT). These two values are low compared to those obtained for the width, suggesting that the inversion of gravity data gives better constraints on the mid-profile location than on the lateral extent of the transition zone.

3.4. Sensitivity to the data uncertainties

In all previous synthetic tests, the inversions were performed with data uncertainties $\sigma_g = 10$ mGal and $\sigma_T = 0.1$ E for the Bouguer anomaly and gravity gradients, respectively. Although these values are generally consistent with our data sets, they can exhibit local changes due to various satellite elevations or relief variations, as well as data sources for the land measurements. Here, to assess the relative contribution of σ_g and σ_T on our inversion results we perform a systematic exploration of the role of the data uncertainties with $\sigma_g \in [5\ mGal; 30\ mGal]$ and $\sigma_T \in [0.01\ E; 0.2\ E]$. We generate a normal distributed random noise with a mean of zero and a standard deviation σ_g or σ_T, which is added to the synthetic data sets calculated from the reference model with $\alpha_{west} = 25$ and $\alpha_{east} = 75$.

Unsurprisingly, our results on gravity and gravity gradients show that data dispersion can affect the standard deviation of the obtained transition zone parameters: the lower the data uncertainties, the lower the standard deviation on the model parameters (Fig. 11). Our results also suggest a greater dependence on the gravity gradient uncertainty than on Bouguer anomaly uncertainty. Indeed, irrespective of the value of σ_g, the standard deviation on model parameters is low if σ_T is small ($\sigma_T < 0.02\ E$). Besides, it can be noted that for the same σ_g and σ_T, the obtained standard deviation differs from one parameter to another. The standard deviation on α_{west} is low (<7) compared to what is obtained for α_{east} (Fig. 11a and b). The location of the western boundary of the

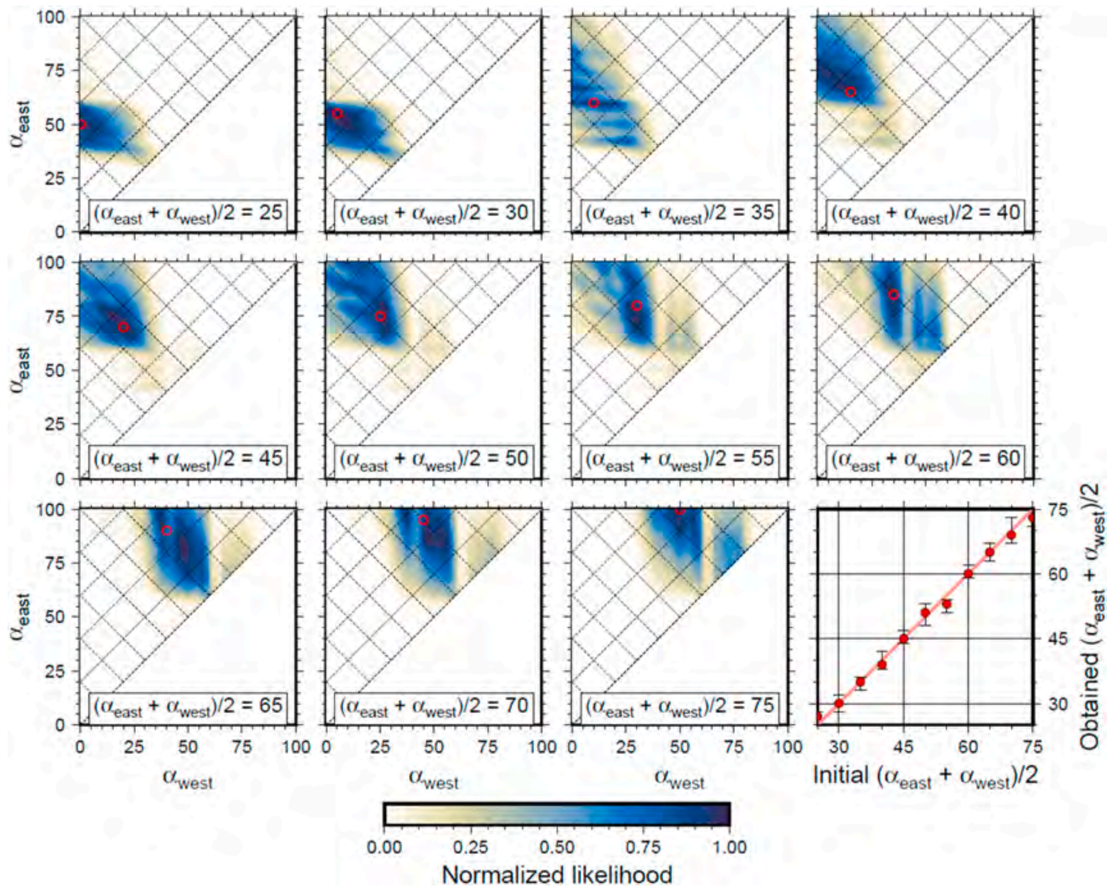

Fig. 10. Synthetic tests assuming for the transition zone a constant width of ca. 250 km ($\alpha_{east} - \alpha_{west} = 50$) and mid-profile located at different positions between central-eastern Nepal ($[\alpha_{east} + \alpha_{west}]/2 = 25$) and westernmost Bhutan ($[\alpha_{east} + \alpha_{west}]/2 = 75$). The color scale shows the calculated likelihood distribution obtained from both gravity gradients and Bouguer anomaly (g_z and T_{ij}) with standard deviations of 0.1 *E* and 10 *mGal*, respectively. The red circle shows the assumed initial coefficients α_{west} and α_{east} of synthetic models. The bottom right figure gives a comparison between the initial and the predicted location of the transition zone. The pink line corresponds to the first bisector ($y = x$).

transition zone thus appears to be better constrained than the eastern one. Likewise, Fig. 11c and d indicates that the standard deviation for the location of the mid-profile is very low (<4; corresponding to ca. 20 km), while for the width it can reach more than 15 (about 75 km). This confirms our finding mentioned in the two previous paragraphs suggesting that the inversion of gravity data sets gives better constraints on the mid-profile location than on the lateral extent of the transition zone.

4. Application to the transition zone between the Nepal and Bhutan segments

In the previous section, our synthetic tests underlined the need to use jointly ground and satellite gravity data. They demonstrated the robustness of our inversion approach and made it possible to estimate its limitations. In the following, we apply this approach to characterize the transition zone between the profiles of Nepal and Bhutan. Due to the lack of information associated with heterogeneous ground gravity datasets and various satellite elevations, we assume a standard deviation of 10 mGal and 0.1 E for the Bouguer anomaly and gravity gradients, respectively.

4.1. Result

As the synthetic tests had shown, the T_{NW} component of satellite gravity gradients is not relevant to constrain the geometry of the study transition zone (Fig. 12). Indeed, the obtained normalized likelihood is relatively constant (between 0.7 and 1) and does not depend on the assumed values of the coefficients α_{west} and α_{east}. On the contrary, the likelihood distributions associated with the other gradients make it possible to better characterize the geometry of this zone (Fig. 12). The inversion of T_{WW} and T_{WZ} gives quite similar likelihood distributions with a α_{west} coefficient ranging between 60 and 75 and a α_{east} coefficient >60. The inversion of the last component T_{ZZ} gives a more complex likelihood distribution. As for T_{WW} and T_{WZ}, it gives a α_{east} coefficient greater than 60, but it also suggests three maxima: one with a very wide lateral extension ($\alpha_{east} - \alpha_{west} > 70$ i.e a width > 350 km), one for which the western boundary is located in easternmost Nepal ($\alpha_{west} \sim 70$), and the last one associated with a narrow transition zone in western-central Bhutan located near Hammer's profile ($\alpha_{west} > 90$).

The inversion of the ground gravity dataset gives very similar results to those obtained for T_{ZZ} (Fig. 12) with $\alpha_{west} > 50$ and with three maxima associated with the following coefficients combinations ($\alpha_{west} \sim 20$ $\alpha_{east} \sim 95$), ($\alpha_{west} \sim 55$ $\alpha_{east} \sim 75$) and ($\alpha_{west} \sim 85$ $\alpha_{east} \sim 88$). Compared to previous studies using Bouguer anomaly, the pattern of likelihood distribution is consistent with the model of transition zone proposed by Hetényi et al. (2016) located on the eastern border of Nepal, and that tentatively drawn by Godin and Harris (2014) through western Bhutan.

The joint inversion of ground and satellite gravity data reduces the nonuniqueness of the gravity inversion by limiting the range of α_{east} and by giving only one maximum for the calculated likelihood. The best-fitting models ($\underline{L(m)}_{g_z \text{ and } T_{ij}} > 0.6$) are obtained for α_{west} between 70 and 79 and α_{east} between 71 and 81 (Fig. 12). The best coefficients combination is ($\alpha_{west} = 76$ $\alpha_{east} = 78$), suggesting a very narrow (ca. 10

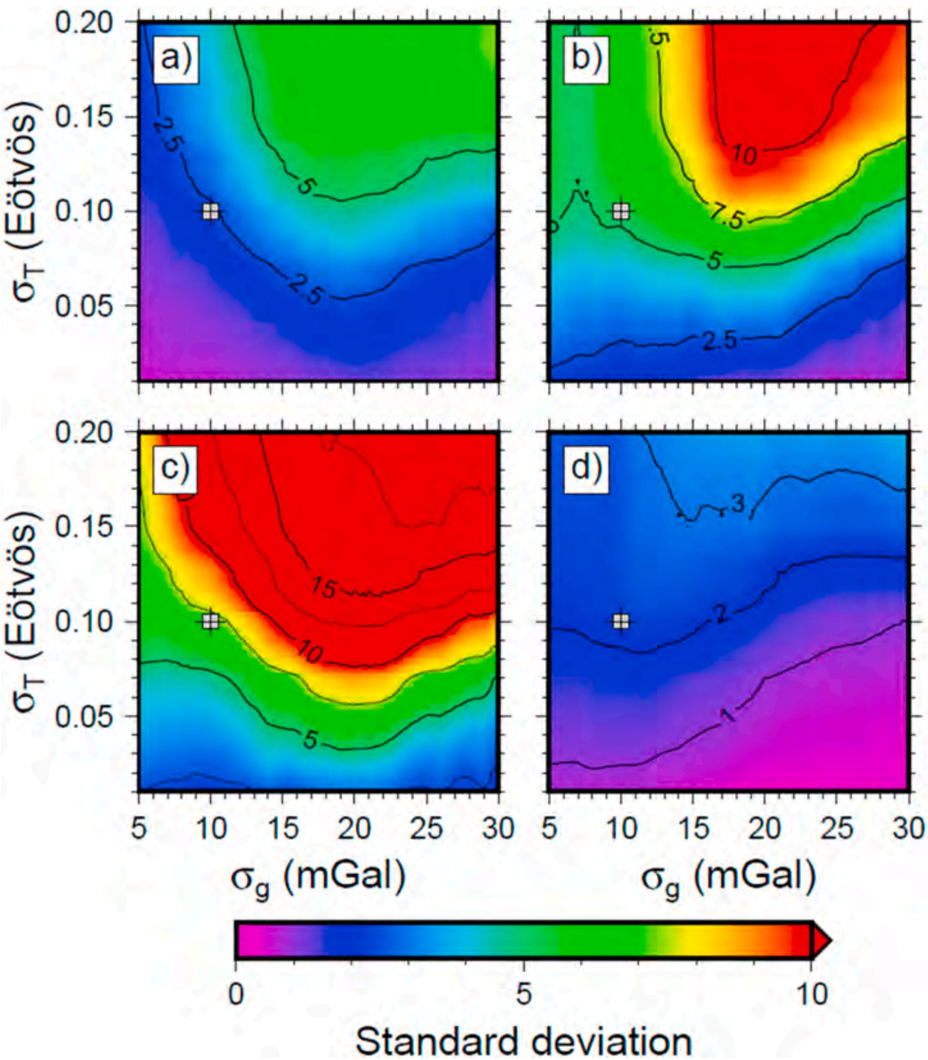

Fig. 11. Synthetic test showing the effect of data dispersion in the variation of predicted coefficients. σ_g and σ_T are the assumed standard deviation of gravity and gravity gradient dataset, respectively. Gray squares indicate the standard deviations of 0.1 E and 10 mGal used in the reference model. Color scale gives the distribution of standard deviation in kilometers of the transition zone parameters: (a) the western boundary α_{west}, (b) the eastern boundary α_{east}, (c) the width $\alpha_{east} - \alpha_{west}$, and (d) the mid-profile location $[\alpha_{east} + \alpha_{west}]/2$.

km wide) transition zone located between Sikkim and the western border of Bhutan.

The calculated gravity field is in good agreement with the observations (Fig. 13). The northward increase of Bouguer anomalies between the Ganga plain and the Tibetan plateau as well as the lateral variations due to the curvature of the Himalayan arc are well explained by our model. At shorter wavelengths, compared to the total signal the average difference between the observed and calculated Bouguer anomaly along the Himalayan arc is low (<50 mGal) suggesting that our models correctly also account for the latitudinal variations between Nepal and Bhutan. Similarly, a good agreement is obtained for the GOCE gravity gradients. The main features of the spatial distribution of gravity gradients are well-retrieved (Fig. 13). The average residual is less than 0.2 E for T_{NW} and T_{ZZ} and reaches up to 0.3 E for T_{WW} and T_{WZ}.

It can be noted that our calculations slightly overestimate the amplitude of both the Bouguer anomaly in central Tibet and the gravity gradients over the entire study area. This could suggest that the density contrasts used in our models are too high, especially under the Tibetan plateau. This could be corrected by changing either the crust-mantle density contrast or the extent of the eclogitized lower crust. Such an approach would require a systematic study, which is however beyond the scope of this paper. Moreover, this correction mainly concerns the northern part of our study area, so it will not significantly modify our findings on the geometry of the transition zone between the segments of Nepal and Bhutan.

At shorter wavelengths, our calculations cannot explain some local variations highlighted by ground gravity data such as those observed in the Ganga plain near longitude 88°. This inconsistency can be related to the approach itself. For the sake of simplicity, in our calculations, we have only used six different densities associated with the sediment foreland basin, the Tibetan crust, and the upper crust, the lower crust (eclogitized beneath Tibet) and the lithospheric mantle of the Indian plate. No density variation within the same layer is therefore taken into account and no local variations of the gravity field can be simulated.

4.2. Discussion

In the northern part of our study area, the 350 km long Pumqu-Xainza rift and the 500 km long Yadong-Gulu rift are the two main tectonic features (Fig. 14). Located in southern and central Tibet, they are already proposed as preexisting weak zones favoring the lithosphere tearing (e.g. Chen et al., 2015; Li and Song, 2018). In southern Tibet, the location of the obtained transition zone coincides with the southernmost part of Yadong-Gulu graben. Besides, its small width and the steeper Indian plate in Bhutan compared to Nepal (Fig. 2) suggest a sub-vertical east-dipping lateral ramp consistent with geological and geophysical observations across the Yadong structure (e.g. Burchfield et al., 1992; Hauck et al., 1998; Zhang et al., 2013; Wang et al., 2017). One can however note the difference in orientation between the obtained transition zone and the NNE-SSW trending Yadong normal faults at the

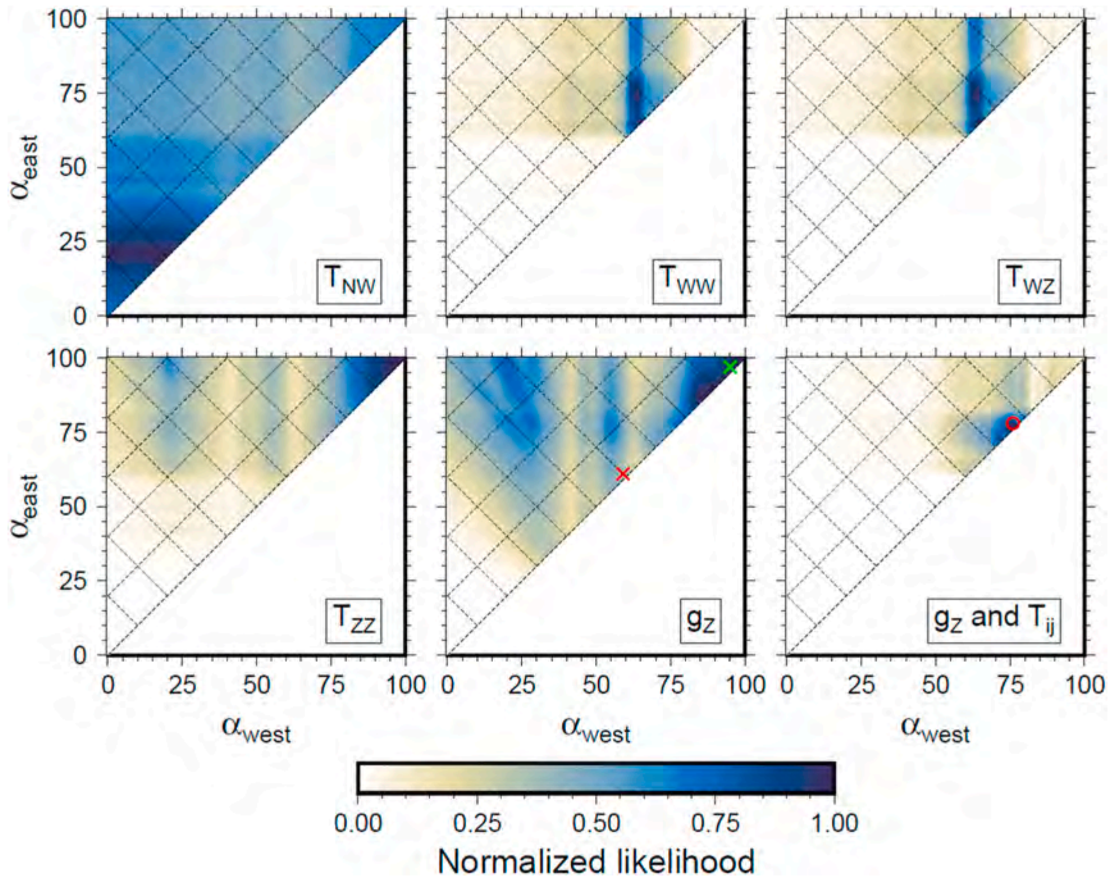

Fig. 12. Normalized likelihood distribution obtained from gravity gradients and Bouguer anomaly observed between central Nepal and western Bhutan (see Fig. 5 and 6). $\sigma_T = 0.1\ E$ and $\sigma_g = 10\ mGal$ are assumed for the standard deviations of gravity gradient and gravity dataset, respectively. The bottom center figure shows the result obtained from Bouguer anomaly. Red and green cross are associated with the models proposed by Hetényi et al. (2016) and Godin and Harris (2014), respectively. The bottom right figure gives the result obtained from both gravity and gravity gradients showing a likelihood maxima with $\alpha_{west} = 76$ and $\alpha_{east} = 78$ (red circle).

western border of Bhutan. This disagreement is related to our approach itself, which is based on the lateral extension of Berthet's section and Hammer's north-south profile and thus allows us to model solely radial transition zones which are north-south trending in Bhutan. However, this limitation does not significantly affect our result suggesting that the Yadong structure controls the segmentation in southern Tibet.

In the Himalaya the location of the obtained transition also coincides with the northern part of the Dhubri–Chungthang fault (DCF). This dextral fault zone has no geomorphological surface expression but is well-constrained by a 20–40 km deep active dextral strike-slip seismicity (Diehl et al., 2017). While the oblique orientation of the DCF cannot be taken into account in our approach using radial profile, our results confirm the finding of Diehl et al. (2017) underlying the key role of the DCF in the segmentation of the downgoing Indian plate.

The southern part of our study area consists of Himalayan foreland basins and Precambrian metamorphic terrains constituting the Indian shield. In our approach, the lateral variation in the depth of sedimentary basins is defined *a priori* (Fig. 2) and is also reflected in field data (Dasgupta et al., 2000, reported in Hetényi et al., 2016 Fig. 4c). It cannot therefore be used to discuss our results. On the contrary, no *a priori* information is given from the location of inherited tectonic structures. They include the Munger-Saharsa ridge and the Shillong plateau visible in the topography of northern India (Fig. 14). The often proposed linkage between the Yadong-Gulu rift and the Munger-Saharsa ridge (e.g. Ni and Barazangi, 1984) suggests that this structure has a key role in the segmentation of Himalaya. However, the obtained transition zone does not coincide with this structure, as it is offset eastwards by > 50 km. Inherited tectonic features also include approximately north-south trending structures as the Pingla and the Kishanganj faults bounding the eastern edge of the Munger-Saharsa ridge, the blind Madhupur fault (also named the Tista fault) in northern Bangladesh (Morgan and McIntire, 1959) and the Dhubri fault located along the western edge of the Shillong Plateau (Fig. 14). The obtained transition zone is located between the Kishanganj and Madhupur active faults. It coincides with the Madhupur fault in the southern edge of Himalaya, but considering the possible deviation in its width (see synthetic tests Fig. 11) as well as its orientation limitation due to our approach, the control of the Kishanganj fault cannot be ruled out. We still favor the most likely model, for which the transition zone between the Nepal and Bhutan segments links the Madhupur fault and the Dhubri–Chungthang fault with the Yadong rift. Recently, Dal Zilio et al. (2020) estimated the spatial distribution of interseismic coupling along the Main Himalayan Thrust, which is the megathrust accommodating most of the shortening across the Himalayan range. In our study area, they obtained a heterogeneous distribution, for which fault patches with low interseismic coupling in eastern Nepal coincide with the Munger-Saharsa ridge. Further east, this coupling remains low until the longitude of the obtained transition zone where we can observe an abrupt increase in coupling consistent with geodetic data in western Bhutan (Marechal et al., 2016). This spatial coincidence strengthens our findings by suggesting the relationship between interseismic coupling zonation and the segmentation of the Himalayan arc proposed by Dal Zilio et al. (2020).

Due to uncertainties in dating past seismic events (which can be several hundred years old), paleoseismic studies performed in our area suggest the occurrence of either (1) a sequence of great M > 8 earthquakes between 1020 and 1520 or (2) a giant earthquake in ca. 1100

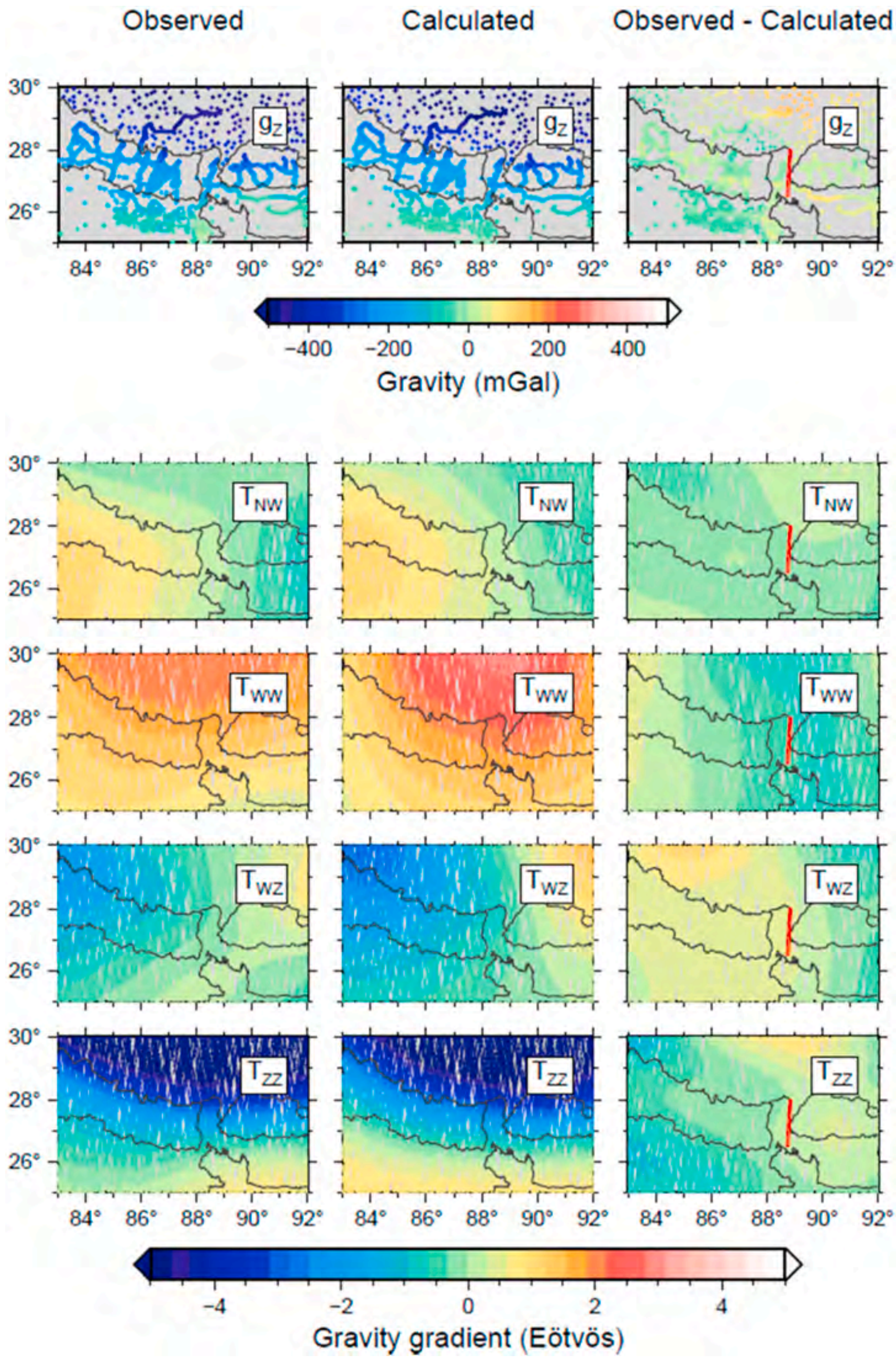

Fig. 13. Comparison between observed and predicted gravity and gravity gradient from central Nepal to western Bhutan. The first column summarizes the observations presented in Fig. 1 and 3. The second column shows the gravity and gravity gradient calculated from our best-fitting model, in which $\alpha_{west} = 76$ and $\alpha_{east} = 78$ ($width \simeq 10\ km$ and $mid-\ profile\ longitude \simeq 88.4°$). The third column shows the difference between the observed and calculated gravity and gravity gradient. The red narrow rectangle gives the location of the obtained transition zone. The same color scale is used to plot observations, predicted fields, and their differences.

which broke more than 700 km distance along the Himalayan arc between central Nepal and eastern Bhutan (Fig. 14). Our approach partly allows us to resolve this question. We obtain an abrupt and narrow transition located near the western boundary of Bhutan. Such a subvertical lateral ramp could act as a barrier to earthquake rupture propagation and thus could restrict the extent of major earthquakes to only one side and therefore a shorter seismic segment. This favors the first scenario presented above, for which the observations between Nepal and Bhutan on either side of the transition zone are unlikely to be linked to the same seismic event. In that case, the paleoseismic studies performed in easternmost Nepal by Nakata et al. (1998), Upreti et al. (2000), and Wesnousky et al. (2017b) can provide key information on the termination of the rupture that affected Nepal in ca. 1100. While this hypothesis remains speculative, it is supported by the low interseismic coupling obtained in this area by Dal Zilio et al. (2020), which leads to a small accumulation of stress to be released during a forthcoming earthquake. Constraints on the location of the M8 earthquake in 1714 in Bhutan (Hetényi et al., 2016b) are also coherent with the transition zone found in this study.

5. Conclusions

Taking advantage of the available information in Nepal and Bhutan, we have developed an inversion approach to explore the along-arc segmentation of the Himalayan belt using mainly gravity data. Synthetic tests demonstrate the effectiveness of the approach to locate the

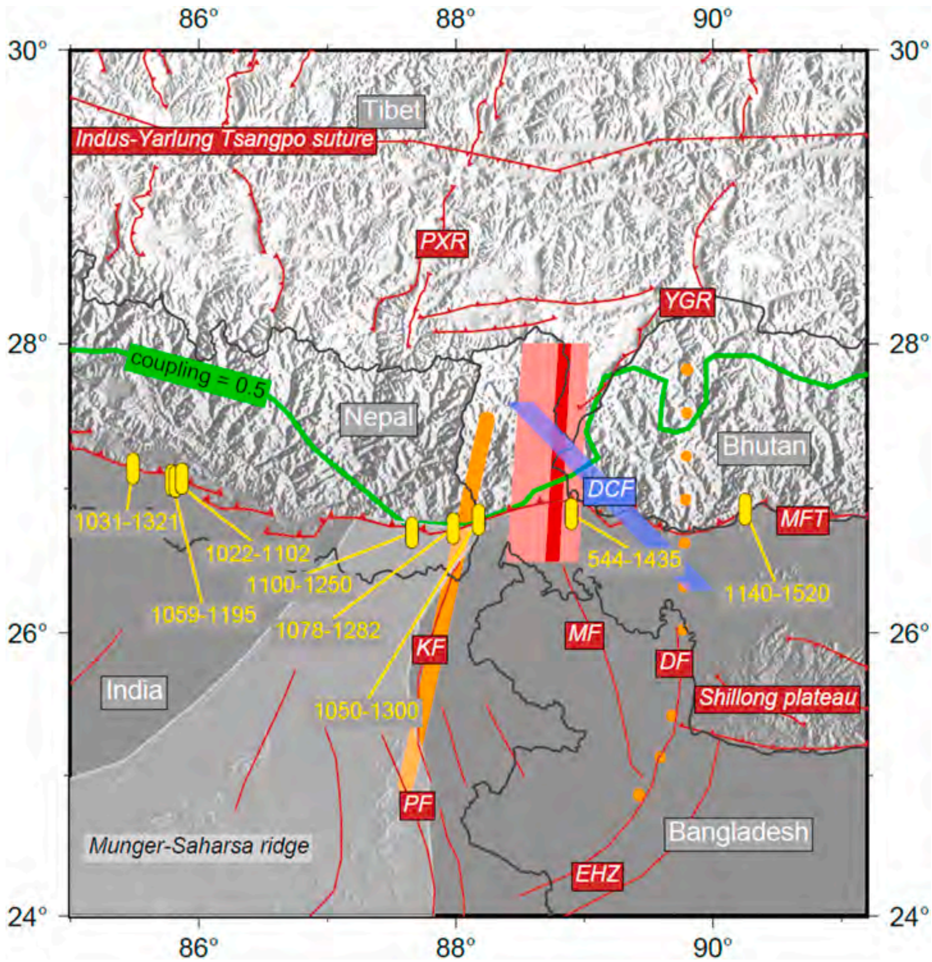

Fig. 14. Map showing the location of the obtained transition zone between the Himalayan segments of Nepal and Bhutan. The red rectangle is associated with the best-fitting model, the pink rectangle represents a variance of 1 sigma. The orange lines are previously proposed segment boundaries by Hetényi et al., (2016) (solid) and Godin and Harris (2014) (dotted). Borders of India, Bangladesh, Nepal, Bhutan, and Tibet as well as major tectonic structures (DCF, Dhubri-Chungthang fault zone highlighted in blue; EHZ, Eocene Hinge Zone, KF, Kishanganj fault; MF, Madhupur fault; MFT, Main Frontal Thrust; PF, Pingla fault; PXR, Pumqu-Xainza rift; YGR, Yadong-Gulu rift; Indus-Yarlung suture) are shown as reference. Yellow rectangles give the location of study sites along the Main Frontal Thrust (MFT) modified from Wesnousky et al. (2019). Sites are labeled with the age range of paleoearthquakes. The green line depicts the contour line of interseismic coupling = 0.5 obtained by Dal Zilio et al. (2020). The light gray shaded patch indicates the extent of the Munger-Saharsa ridge.

two edges of the transition zone between the segments of the central and the eastern Himalaya. Irrespective of the location along the Himalayan arc and the lateral extent of this transition zone, these two parameters are found with a standard deviation $< 0.2°$ longitude along the MFT and ca. 35 km in width. Synthetic tests also underline the need for joint inversion of both Bouguer anomaly measurements and GOCE gravity gradient observations to reduce the nonuniqueness of gravity inversions.

The joint inversion of ground and satellite data sets suggest a ca. 10 km wide transition zone located at the western border of Bhutan. Compared to previous studies using Bouguer anomaly only, this transverse tectonic feature is between the location proposed by Hetényi et al. (2016) on the eastern border of Nepal, and that proposed by Godin and Harris (2014) through western Bhutan. This abrupt segmentation is supported by structural observations and could be related to the Madhupur fault in the foreland, the Dhubri–Chungthang fault cutting the India plate beneath Himalaya and the Yadong-Gulu rift in southern Tibet.

The obtained transition zone is narrow enough to possibly prevent seismic rupture propagation across this boundary between Nepal and Bhutan. This could result in the seismic segmentation of the Main Himalayan Thrust and potentially restrict the size of large earthquakes along the Himalayan belt. Such information are essential inputs of seismic hazard models, as they delimit the extent of possible fault sources. The more precise location, geometry and nature of this and other transitions in the Himalaya – whether it is a ramp, a fault, or other feature, – should be investigated in the future. Forthcoming research will hence contribute to improve existing probabilistic seismic hazard models of Northern India, Nepal (Stevens et al., 2018) and Bhutan (Stevens et al., 2020).

Credit author statement

Cattin, Conceptualization, Methodology, Software, Validation, Formal analysis, Investigation, Data curation, Writing – original draft, Writing – review & editing, Visualization, Supervision, Project administration, Funding acquisition. Berthet, Conceptualization, Data curation, Writing – review & editing, Visualization. Hetényi, Conceptualization, Data curation, Writing – original draft, Writing – review & editing, Visualization, Funding acquisition. Saraswati, Software, Investigation, Data curation, Writing – review & editing. Panet, Conceptualization, Resources, Data curation, Writing – review & editing. Mazzotti, Conceptualization, Writing – review & editing. Cadio, Writing – review & editing. Ferry, Writing – review & editing.

Declaration of competing interest

The authors declare that they have no known competing financial interests or personal relationships that could have appeared to influence the work reported in this paper.

Acknowledgments

The authors acknowledge the comments and helpful suggestions of the editor Sebastiano D'Amico and two anonymous reviewers that helped to improve the manuscript. This work was supported by grants from the Agence National de la Recherche ANR-18-CE01-0017 and CNES TOSCA, as well as the Swiss National Science Foundation grant PP00P2_157627 (project OROG3NY). The figures of this paper were prepared using the Generic Mapping Tools version 6 (Wessel et al.,

2019).

References

Banerjee, P., 1998. Gravity measurements and terrain corrections using a digital terrain model in the NW Himalaya. Comput. Geosci. 24, 1009–1020.

Berthet, T., Hetényi, G., Cattin, R., Sapkota, S.N., Champollion, C., Kandel, T., Doerflinger, E., Drukpa, D., Lechmann, S., Bonin, M., 2013. Lateral similarity of India plate strength and crustal structure over Central and Eastern Nepal. Geophy. J. Int. 195, 1481–1493. https://doi.org/10.1093/gji/ggt357.

Bollinger, L., Sapkota, S.N., Tapponnier, P., Klinger, Y., Rizza, M., Van Der Woerd, J., Tiwari, D.R., Pandey, R., Bitri, A., Bes de Berc, S., 2014. Estimating the return times of great himalayan earthquakes in eastern Nepal: evidence from the patu and bardibas strands of the main frontal thrust. J. Geophys. Res.: Solid Earth 119 (9), 7123–7163.

Burchfiel, B.C., Zhiliang, C., Hodges, K.V., Yuping, L., Royden, L.H., Changrong, D., 1992. The South Tibetan detachment system. Himalayan orogen: Extension contemporaneous with and parallel to shortening in a collisional mountain belt 269 (Geological Society of America).

Cattin, R., Mazzotti, S., Baratin, L.M., 2015. GravProcess: an easy-to-use MATLAB software to process campaign gravity data and evaluate the associated uncertainties. Comput. Geosci. 81, 20–27.

Chen, Y., Li, W., Yuan, X., Badal, J., Teng, J., 2015. Tearing of the Indian lithospheric slab beneath southern Tibet revealed by SKS-wave splitting measurements. Earth Planet Sci. Lett. 413, 13–24.

Coutand, I., Whipp Jr., D.M., Grujic, D., Bernet, M., Fellin, M.G., Bookhagen, B., Landry, K.R., Ghalley, S.K., Duncan, C., 2014. Geometry and kinematics of the Main Himalayan Thrust and Neogene crustal exhumation in the Bhutanese Himalaya derived from inversion of multithermochronologic data. J. Geophys. Res. Solid Earth 119, 1446–1481. https://doi.org/10.1002/2013JB010891.

Dal Zilio, L., Jolivet, R., van Dinther, Y., 2020. Segmentation of the main himalayan thrust illuminated by bayesian inference of interseismic coupling. Geophys. Res. Lett. 47 e2019GL086424.

Das, D., Mehra, G., Rao, K.G.C., Roy, A.L., Narayana, M.S., 1979. Bouguer, free-air and magnetic anomalies over northwestern Himalaya. Himalayan geology seminar, section III, oil and natural gas Resources. Geol. Surv. India Misc. Publ. 41, 141–148.

Dasgupta, S., et al., 2000. In: Narula, P.L., Acharyya, S.K., Banerjee, J. (Eds.), Seismotectonic Atlas of India and its Environs. Geological Survey of India, Calcutta, India, p. 87.

Diehl, T., Singer, J., Hetényi, G., Grujic, D., Clinton, J., Giardini, D., Kissling, E., Gansser Working Group, 2017. Seismotectonics of Bhutan: evidence for segmentation of the Eastern Himalayas and link to foreland deformation. Earth Planet Sci. Lett. 471, 54–64.

Duncan, C., Masek, J., Fielding, E., 2003. How steep are the Himalaya? Characteristics and implications of along-strike topographic variations. Geology 31, 75–78. https://doi.org/10.1130/0091-7613.

Fuchs, M., Bouman, J., 2011. Rotation of GOCE gravity gradients to local frames. Geophys. J. Int. 187, 743–753.

Godin, L., Harris, L.B., 2014. Tracking basement cross-strike discontinuities in the Indian crust beneath the Himalayan orogen using gravity data–relationship to upper crustal faults. Geophys. J. Int. 198 (1), 198–215.

Gahalaut, V.K., Arora, B.R., 2012. Segmentation of seismicity along the Himalayan Arc due to structural heterogeneities in the under-thrusting Indian plate and overriding Himalayan wedge. Episodes 35 (4), 493–500.

Gruber, T., Visser, P.N., Ackermann, C., Hosse, M., 2011. Validation of GOCE gravity field models by means of orbit residuals and geoid comparisons. J. Geodes. 85 (11), 845–860.

Hammer, P., Berthet, T., Hetényi, G., Cattin, R., Drukpa, D., Chophel, J., Lechmann, S., Moigne, N.L., Champollion, C., Doerflinger, E., 2013. Flexure of the India plate underneath the Bhutan Himalaya. Geophys. Res. Lett. 40 (16), 4225–4230.

Hauck, M.L., Nelson, K.D., Brown, L.D., Zhao, W., Ross, A.R., 1998. Crustal structure of the Himalayan orogen at∼ 90 east longitude from Project INDEPTH deep reflection profiles. Tectonics 17 (4), 481–500.

Hetényi, G., Cattin, R., Brunet, F., Vergne, J., Bollinger, L., Nábělek, J.L., Diament, M., 2007. Density distribution of the India plate beneath the Tibetan Plateau: geophysical and petrological constraints on the kinetics of lower-crustal eclogitization. Earth Planet Sci. Lett. 264, 226–244. https://doi.org/10.1016/j.epsl.2007.09.036.

Hetényi, G., Cattin, R., Berthet, T., Le Moigne, N., Chophel, J., Lechmann, S., Hammer, P., Drukpa, D., Sapkota, S.N., Gautier, S., Thinley, K., 2016. Segmentation of the Himalayas as revealed by arc-parallel gravity anomalies. Sci. Rep. 6 (1), 1–10.

Hetényi, G., Le Roux-Mallouf, R., Berthet, T., Cattin, R., Cauzzi, C., Phuntsho, K., Grolimund, R., 2016b. Joint approach combining damage and paleoseismology observations constrains the 1714 A.D. Bhutan earthquake at magnitude 8±0.5. Geophys. Res. Lett. 43, 10695–10702. https://doi.org/10.1002/2016GL071033.

Kumar, S., Wesnousky, S.G., Jayangondaperumal, R., Nakata, T., Kumahara, Y., Singh, V., 2010. Paleoseismological evidence of surface faulting along the northeastern Himalayan front, India: timing, size, and spatial extent of great earthquakes. J. Geophys. Res. 115 (B12), B12422.

Lavé, J., Yule, D., Sapkota, S., Basant, K., Madden, C., Attal, M., Pandey, R., 2005. Evidence for a great Medieval earthquake (∼ 1100 AD) in the central Himalayas, Nepal. Science 307 (5713), 1302–1305.

Le Roux-Mallouf, R., Godard, V., Cattin, R., Ferry, M., Gyeltshen, J., Ritz, J.F., Drupka, D., Guillou, V., Arnold, M., Aumaître, G., Bourlès, D.L., 2015. Evidence for a wide and gently dipping Main Himalayan Thrust in western Bhutan. Geophys. Res. Lett. 42 (9), 3257–3265.

Le Roux-Mallouf, R., Ferry, M., Ritz, J.-F., Berthet, T., Cattin, R., Drukpa, D., 2016. First paleoseismic evidence for great surface-rupturing earthquakes in the Bhutan Himalayas. J. Geophys. Res. Solid Earth 121. https://doi.org/10.1002/2015JB012733.

Le Roux-Mallouf, R., Ferry, M., Cattin, R., Ritz, J.F., Drukpa, D., Pelgay, P., 2020. A 2600-yr-long paleoseismic record for the himalayan main frontal thrust (western Bhutan). Solid Earth 11, 2359–2375.

Le Fort, P., 1975. Himalaya: the collided range. Present knowledge of the continental arc. Am. J. Sci. 275A, 1–44.

Li, J., Song, X., 2018. Tearing of Indian mantle lithosphere from high-resolution seismic images and its implications for lithosphere coupling in southern Tibet. Proc. Natl. Acad. Sci. Unit. States Am. 115 (33), 8296–8300.

Marechal, A., Mazzotti, S., Cattin, R., Cazes, G., Vernant, P., Drukpa, D., Tninley, K., Tarayoun, A., Le Roux-Mallouf, R., Thapa, B.B., Pelgay, P., Gyeltshen, J., Doerflinger, E., Gautier, S., 2016. Evidence of interseismic coupling variations along the Bhutan Himalayan arc from new GPS data. Geophys. Res. Lett. 43 (24), 12–399.

Martelet, G., Sailhac, P., Moreau, F., Diament, M., 2001. Characterization of geological boundaries using 1-D wavelet transform on gravity data: theory and application to the Himalayas. Geophysics 66, 1116–1129.

McQuarrie, N., Robinson, D., Long, S., Tobgay, T., Grujic, D., Gehrels, G., Ducea, M., 2008. Preliminary stratigraphic and structural architecture of Bhutan: implications for the along strike architecture of the Himalayan system. Earth Planet Sci. Lett. 272, 105–117. https://doi.org/10.1016/j.epsl.2008.04.030.

McQuarrie, N., Ehlers, T.A., 2015. Influence of thrust belt geometry and shortening rate on thermochronometer cooling ages: insights from thermokinematic and erosion modeling of the Bhutan Himalaya. Tectonics 34, 1055–1079. https://doi.org/10.1002/2014TC003783.

Morgan, J.P., McIntire, W.G., 1959. Quaternary geology of the bengal basin, east Pakistan and India. Geol. Soc. Am. Bull. 70 (3), 319–342.

Mugnier, J.-L., Gajurel, A., Huyghe, P., Jayangandaperumal, R., Jouanne, F., Upreti, B., 2013. Structural interpretation of the great earthquakes of the last millennium in the central Himalaya. Earth Sci. Rev. https://doi.org/10.1016/j.earscirev.2013.09.003.

Nábělek, J., Hetényi, G., Vergne, J., Sapkota, S., Kafle, B., Jiang, M., Su, H., Chen, J., Huang, B.S., 2009. Underplating in the Himalaya-Tibet collision zone revealed by the Hi-CLIMB experiment. Science 325 (5946), 1371–1374.

Nakata, T., Kumura, K., Rockwell, T., 1998. First successful paleoseismic trench study on active faults in the Himalaya. Eos Trans. AGU 79, 45.

Ni, J., Barazangi, M., 1984. Seismotectonics of the Himalayan collision zone: geometry of the underthrusting Indian plate beneath the Himalaya. J. Geophys. Res.: Solid Earth 89 (B2), 1147–1163.

Rajendran, C.P., John, B., Rajendran, K., 2015. Medieval pulse of great earthquakes in the central Himalaya: viewing past activities on the frontal thrust. J. Geophys. Res.: Solid Earth 120 (3), 1623–1641.

Robert, X., Van Der Beek, P., Braun, J., Perry, C., Mugnier, J.-L., 2011. Control of detachment geometry on lateral variations in exhumation rates in the Himalaya: insights from low-temperature thermochronology and numerical modeling. J. Geophys. Res. 116, B05202. https://doi.org/10.1029/2010JB007893.

Sapkota, S.N., Bollinger, L., Klinger, Y., Tapponnier, P., Gaudemer, Y., Tiwari, D., 2013. Primary surface ruptures of the great Himalayan earthquakes in 1934 and 1255. Nat. Geosci. 6 (1), 71–76.

Saraswati, A.T., Cattin, R., Mazzotti, S., Cadio, C., 2019. New analytical solution and associated software for computing full-tensor gravitational field due to irregularly shaped bodies. J. Geodes. 93 (12), 2481–2497.

Schulte-Pelkum, V., Monsalve, G., Sheehan, A., Pandey, M.R., Sapkota, S., Bilham, R., Wu, F., 2005. Imaging the Indian subcontinent beneath the Himalaya. Nature 435 (7046), 1222–1225.

Singer, J., Kissling, E., Diehl, T., Hetényi, G., 2017. The underthrusting Indian crust and its role in collision dynamics of the Eastern Himalaya in Bhutan: insights from receiver function imaging. J. Geophys. Res. Solid Earth 122, 1152–1178. https://doi.org/10.1002/2016JB013337.

Stevens, V.L., Shrestha, S.N., Maharjan, D.K., 2018. Probabilistic seismic hazard assessment of Nepal. Bull. Seismol. Soc. Am. 108 (6), 3488–3510.

Stevens, V.L., De Risi, R., Le Roux-Mallouf, R., Drukpa, D., Hetényi, G., 2020. Seismic hazard and risk in Bhutan. Nat. Hazards 104 (3), 2339–2367.

Sun, W., 1989. Bouguer gravity anomaly map of the people's Republic of China. Chin. Acad. Geoexploration. Beijing.

Tiwari, V.M., Vyghreswara, R., Mishra, D.C., Singh, B., 2006. Crustal structure across Sikkim, NE Himalaya from new gravity and magnetic data. Earth Planet Sci. Lett. 247, 61–69.

Upreti, B.N., Nakata, T., Kumahara, Y., Yagi, H., Okumura, K., Rockwell, T.K., Virdi, N.S., 2000. The latest active faulting in Southeast Nepal. In: Proceedings of the Hokudan International Symposium and School in Active Faulting. Awaji Island, Hyogo Japan, pp. 533–536.

Wang, G., Wei, W., Ye, G., Jin, S., Jing, J., Zhang, L., Dong, H., Xie, C., Omisore, B.O., Guo, Z., 2017. 3-D electrical structure across the Yadong-Gulu rift revealed by magnetotelluric data: new insights on the extension of the upper crust and the geometry of the underthrusting Indian lithospheric slab in southern Tibet. Earth Planet Sci. Lett. 474, 172–179.

Wesnousky, S.G., Kumahara, Y., Chamlagain, D., Pierce, I.K., Karki, A., Gautam, D., 2017a. Geological observations on large earthquakes along the Himalayan frontal fault near Kathmandu, Nepal. Earth Planet Sci. Lett. 457, 366–375.

Wesnousky, S.G., Kumahara, Y., Chamlagain, D., Pierce, I.K., Reedy, T., Angster, S.J., Giri, B., 2017b. Large paleoearthquake timing and displacement near Damak in eastern Nepal on the Himalayan Frontal Thrust. Geophys. Res. Lett. 44, 8219–8226.

Wesnousky, S.G., Kumahara, Y., Nakata, T., Chamlagain, D., Neupane, P., 2018. New observations disagree with previous interpretations of surface rupture along the himalayan frontal thrust during the great 1934 Bihar-Nepal Earthquake. Geophys. Res. Lett. 45, 2652–2658.
Wesnousky, S.G., Kumahara, Y., Chamlagain, D., Neupane, P.C., 2019. Large himalayan frontal thrust paleoearthquake at khayarmara in eastern Nepal. J. Asian Earth Sci. 174, 346–351.
Wessel, P., Luis, J.F., Uieda, L., Scharroo, R., Wobbe, F., Smith, W.H.F., Tian, D., 2019. The generic mapping tools version 6. G-cubed 20 (11), 5556–5564.
Zhang, Z., Chen, Y., Yuan, X., Tian, X., Klemperer, S.L., Xu, T., Bai, Z., Zhang, H., Wu, J., Teng, J., 2013. Normal faulting from simple shear rifting in South Tibet, using evidence from passive seismic profiling across the Yadong-Gulu Rift. Tectonophysics 606, 178–186.